ELSEVIER

Sensors and Actuators A 91 (2001) 278–291

SENSORS AND ACTUATORS A PHYSICAL

www.elsevier.nl/locate/sna

Linear, nonlinear and mixed-regime analysis of electrostatic MEMS

Gang Li[1], N.R. Aluru[*,2]

Beckman Institute for Advanced Science and Technology, University of Illinois at Urbana-Champaign, Urbana, IL 61801, USA

Abstract

Electrostatically actuated microstructures can undergo large deformations for certain geometric configurations and applied voltages. The use of linear theories in such cases can produce inaccurate results. By selecting a range of geometric parameters (such as beam lengths, thicknesses and gaps), we identify the regimes, where linear theories become inaccurate and necessitate the use of nonlinear theories. In cases where linear theories produce inaccurate results, we propose a mixed-regime approach to combine linear and nonlinear theories. We show that a mixed-regime approach can be more efficient compared to a full nonlinear simulation of the electrostatically actuated structure. This paper also proposes the use of meshless techniques for efficient simulation of linear and nonlinear behavior in electrostatic MEMS.

Keywords: Electrostatic MEMS; Linear and nonlinear theories; Meshless method; Mixed-regime approach

1. Introduction

Accurate analysis of electrostatic microelectromechanical systems (MEMS) [1,2] and the development of reliable reduced-order models (or macro-models) [3,4] for rapid system level analysis requires proper understanding and characterization of the nonlinearity in electrostatic devices. The use of linear theories instead of nonlinear theories can produce inaccurate results and the use of nonlinear theories, in situations where linear theories are accurate, can be very expensive and time consuming. Hence, it is critical to identify the regimes where linear and nonlinear theories are valid. In this paper, we focus on identifying the regimes, where linear and nonlinear theories are accurate for electrostatically actuated structures, e.g. electrostatically actuated cantilever and fixed–fixed beams. In particular, we investigate the role of geometric parameters such as the length, width, and thickness of the beam and the gap between the beam and the ground plane in determining the regimes, where linear and nonlinear theories are accurate.

Simulation of nonlinear behavior in electrostatic devices using classical finite-difference [5] and finite-element methods [6] can be very inefficient because of complex meshing requirements. Meshless techniques [7–9] are extremely powerful numerical methods as they do not require the generation of a mesh for complex two- and three-dimensional micromechanical devices. Meshless techniques radically simplify the computer-aided design for MEMS and significantly reduce the design cycle time for innovative MEMS. In this paper, we present a finite cloud method [7] for analysis of electrostatic devices. The key features of the method are: (1) it is a true meshless technique which means that only points need to be sprinkled and no connectivity information among the points is necessary; (2) it uses a fixed kernel approximation for construction of meshless interpolation functions and (3) it uses a collocation method for discretizing the governing partial-differential equations. In this paper, the finite cloud method is extended for geometrically nonlinear analysis of micromechanical structures and an advantage of the finite cloud method over the classical finite element method [10] is it avoids problems with mesh distortion for large deformation analysis.

The peak deflection and pull-in voltage obtained with linear and nonlinear analysis for a cantilever and a fixed–fixed beam with various lengths, thicknesses and gaps are studied. It is shown that for a small gap, both linear and nonlinear theories give identical results, which are in excellent agreement with published data [11] for pull-in voltages. However, as the gap increases, with all other variables held fixed, significant deviations are observed between linear and nonlinear theories. Specifically, we have observed that for larger gaps in comparison with the length (e.g.

* Corresponding author.
E-mail address: aluru@uiuc.edu (N.R. Aluru).
[1] Doctoral student, Department of Mechanical and Industrial Engineering and Beckman Institute.
[2] Assistant professor, Department of General Engineering and Beckman Institute.

0924-4247/01/$ – see front matter
PII: S0924-4247(01)00597-0

for gap/length ratio greater than 30% in cantilever beam case), the pull-in voltages obtained with nonlinear theories are accurate, and the linear theories are in significant error. For larger gaps, where the deviations between linear and nonlinear results are significant, we observe that up to a certain applied voltage (defined as V_l), the deflection obtained with the linear and nonlinear results is identical. It is for applied voltages beyond V_l, where the deviations between linear and nonlinear results are observed. We propose a new approach, referred to as a mixed-regime approach, where a linear analysis is employed upto V_l and a nonlinear analysis is employed beyond V_l. Compared to a full nonlinear analysis, a mixed-regime approach is less expensive with no deterioration in accuracy.

The rest of the paper is organized as follows. In Section 2 we summarize the governing equations for small and large deformation analysis of micromechanical structures. The construction of meshless interpolation functions in a finite cloud method is summarized in Section 3. The use of the finite cloud method for linear and nonlinear analysis is summarized in Sections 4 and 5, respectively. Results on linear and nonlinear analysis of electromechanical devices are given in Section 6 and the mixed-regime approach is presented in Section 7. Finally, conclusions are given in Section 8.

2. Governing equations

We will be primarily concerned with two-dimensional devices in this paper. For small micro-mechanical deformations, the linear theory of elasticity as defined by Eqs. (1)–(3) can be used [12].

$$\nabla \cdot (\tau) + \boldsymbol{b} = 0 \text{ in } \Omega \tag{1}$$

$$\boldsymbol{u} = \boldsymbol{g} \text{ in } \Gamma_g \tag{2}$$

$$\tau \cdot \boldsymbol{n} = \boldsymbol{h} \text{ in } \Gamma_h \tag{3}$$

where τ is the Cauchy stress tensor, $\boldsymbol{b}$ the body force vector, $\boldsymbol{u}$ the displacement vector, $\boldsymbol{g}$ the specified displacement vector on the boundary portion Γ_g, $\boldsymbol{h}$ the surface traction vector on the boundary Γ_h and $\boldsymbol{n}$ the unit outward normal vector. In coupled electro-mechanical analysis, the surface tractions are nothing but the electrostatic forces. When the electrostatic forces are dominant, the micro-mechanical structure can undergo large deformation, in which case the linear theory described in Eqs. (1)–(3) may produce inaccurate results.

When an elastic body undergoes large deformation, the difference between the initial configuration and the deformed configuration can not be neglected as was done for the case of linear elasticity. For geometrically nonlinear analysis, the second Piola–Kirchhoff stress and the Green–Lagrangian strain are used as the stress and the strain measures, respectively. The governing equations for large deformation analysis using a total Lagrangian description are given as follows [12].

$$\nabla \cdot (\boldsymbol{FS}) + \boldsymbol{B} = 0 \text{ in } \Omega \tag{4}$$

$$\boldsymbol{u} = \boldsymbol{G} \text{ in } \Gamma_g \tag{5}$$

$$\boldsymbol{P} \cdot \boldsymbol{N} = \boldsymbol{H} \text{ in } \Gamma_h \tag{6}$$

where $\boldsymbol{F}$ is the deformation gradient.

$$\boldsymbol{F} = \boldsymbol{I} + \nabla \boldsymbol{u} \tag{7}$$

where $\boldsymbol{u}$ is the displacement vector from the initial configuration $\boldsymbol{X}$ to the deformed configuration $\boldsymbol{x}$, $\boldsymbol{x} = \boldsymbol{X} + \boldsymbol{u}$, $\boldsymbol{I}$ identity tensor, $\boldsymbol{N}$ the unit outward normal vector in the initial configuration and $\boldsymbol{S}$ the second Piola–Kirchhoff stress given by

$$\boldsymbol{S} = \boldsymbol{CE} \tag{8}$$

where $\boldsymbol{C}$ is the material tensor and $\boldsymbol{E}$ the Green–Lagrangian strain.

$$\boldsymbol{E} = \tfrac{1}{2}(\boldsymbol{F}^T\boldsymbol{F} - \boldsymbol{I}) \tag{9}$$

where $\boldsymbol{B}$ is the body force vector per unit undeformed volume, $\boldsymbol{G}$ the prescribed displacement vector and $\boldsymbol{H}$ the surface traction vector per unit undeformed area. $\boldsymbol{P}$ is the first Piola–Kirchhoff stress tensor given by

$$\boldsymbol{P} = \boldsymbol{FS} \tag{10}$$

3. Finite cloud meshless method

The finite cloud meshless method (FCM) uses a fixed kernel approximation [7] to construct the meshless interpolation functions and a point collocation technique [8] to discretize the governing partial differential equations. In the following, we outline the steps used for the construction of interpolation functions (see [7] for more details). The domain is first represented by a set of points (or nodes), as shown in Fig. 1. Then, for each node, an interpolation function is generated by constructing a cloud about that node (also referred to as a star node). A cloud is constructed by centering a kernel about the star point. The kernel is typically a cubic spline or a Gaussian function. The kernel is non-zero at the star point and at a few other nodes that are in the vicinity of the star point. The shape of the cloud, which defines the nodes at which the kernel is non-zero, can be arbitrary. Typical shapes we have employed are circles and rectangles in two-dimension. In a meshless fixed kernel approach, an approximation $u^a(x, y)$ to an unknown $u(x, y)$ is given by

$$u^a(x, y) = \int_\Omega C(x, y, s, t)\phi(x_k - s, y_k - t)u(s, t)\,ds\,dt \tag{11}$$

where $C(x, y, s, t)$ is the correction function which is given by

$$C(x, y, s, t) = \boldsymbol{P}^T(s, t)\boldsymbol{C}(x, y) \tag{12}$$

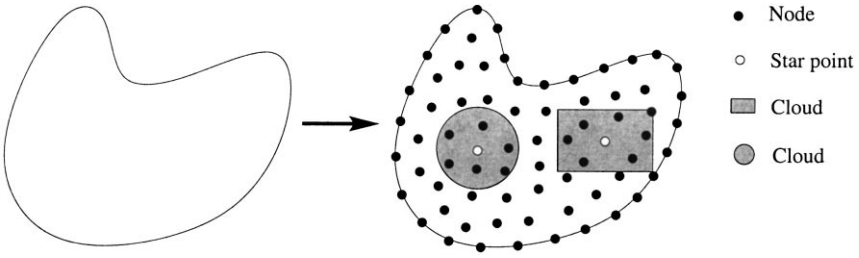

Fig. 1. Physical domain (left) is represented by a set of points (right), clouds are constructed at each point. Also shown in the figure are a circular and a rectangular cloud.

where ϕ is the kernel function which is centered at (x_k, y_k). In this paper, ϕ is taken as a cubic spline function, i.e.

$$\phi(z) = \begin{cases} 0 & z < -2 \\ (z)^3/6 & -2 \le z \le -1 \\ 2/3 - z^2(1 + z/2) & -1 \le z \le 0 \\ 2/3 - z^2(1 - z/2) & 0 \le z \le 1 \\ -(z)^3/6 & 1 \le z \le 2 \\ 0 & z > 2 \end{cases} \tag{13}$$

$\boldsymbol{P} = \{p_1, p_2, \ldots, p_m\}$ is an $m \times 1$ vector of basis functions

$$\boldsymbol{P}^{\mathrm{T}} = \begin{cases} [1, s, t] & m = 3 \\ [1, s, t, s^2, st, t^2] & m = 6 \end{cases} \tag{14}$$

where $\boldsymbol{C}(x, y)$ is an $m \times 1$ vector of unknown correction function coefficients. The correction function coefficients are computed by satisfying the consistency conditions, i.e.

$$\int_{\Omega} \boldsymbol{P}^{\mathrm{T}}(s, t)\boldsymbol{C}(x, y)\phi(x_k - s, y_k - t)p_i(s, t)\,\mathrm{d}s\,\mathrm{d}t = p_i(x, y), \quad i = 1, 2, \ldots, m \tag{15}$$

In discrete form, Eq. (15) can be written as

$$\sum_{I=1}^{\mathrm{NP}} \boldsymbol{P}^{\mathrm{T}}(x_I, y_I)\boldsymbol{C}(x, y)\phi(x_k - x_I, y_k - y_I)p_i(x_I, y_I)\Delta V_I = p_i(x, y), \quad i = 1, 2, \ldots, m \tag{16}$$

where NP is the number of points in the domain and ΔV_I is the nodal volume of node I. Eq. (16) can be written in a matrix form as

$$\boldsymbol{M}\boldsymbol{C}(x, y) = \boldsymbol{P}(x, y) \tag{17}$$

$$M_{ij} = \sum_{I=1}^{\mathrm{NP}} p_i(x_I, y_I)\phi(x_k - x_I, y_k - y_I)p_j(x_I, y_I)\Delta V_I, \quad i, j = 1, 2, \ldots, m \tag{18}$$

From Eq. (17), the unknown correction function coefficients are computed as

$$\boldsymbol{C}(x, y) = \boldsymbol{M}^{-1}\boldsymbol{P}(x, y) \tag{19}$$

Substituting the correction function coefficients into Eq. (11) and employing a discrete approximation for Eq. (11), we obtain

$$u^{\mathrm{a}}(x, y) = \sum_{I=1}^{\mathrm{NP}} N_I(x, y)\hat{u}_I \tag{20}$$

where $\hat{u}_I$ is the nodal parameter for node I, and $N_I(x, y)$ is the fixed kernel meshless interpolation function defined as

$$N_I(x, y) = \boldsymbol{P}^{\mathrm{T}}(x, y)\boldsymbol{M}^{-1}\boldsymbol{P}(x_I, y_I)\phi(x_k - x_I, y_k - y_I)\Delta V_I \tag{21}$$

The derivatives of the unknown u are approximated by

$$\frac{\partial u^{\mathrm{a}}(x, y)}{\partial x} = \sum_{I=1}^{\mathrm{NP}} \frac{\partial N_I(x, y)}{\partial x}\hat{u}_I \tag{22}$$

$$\frac{\partial u^{\mathrm{a}}(x, y)}{\partial y} = \sum_{I=1}^{\mathrm{NP}} \frac{\partial N_I(x, y)}{\partial y}\hat{u}_I \tag{23}$$

$$\frac{\partial^2 u^{\mathrm{a}}(x, y)}{\partial x^2} = \sum_{I=1}^{\mathrm{NP}} \frac{\partial^2 N_I(x, y)}{\partial x^2}\hat{u}_I \tag{24}$$

$$\frac{\partial^2 u^{\mathrm{a}}(x, y)}{\partial y^2} = \sum_{I=1}^{\mathrm{NP}} \frac{\partial^2 N_I(x, y)}{\partial y^2}\hat{u}_I \tag{25}$$

$$\frac{\partial^2 u^{\mathrm{a}}(x, y)}{\partial x \partial y} = \sum_{I=1}^{\mathrm{NP}} \frac{\partial^2 N_I(x, y)}{\partial x \partial y}\hat{u}_I \tag{26}$$

After the interpolation functions are constructed, FCM uses a point collocation technique to discretize the governing equations. In point collocation, the governing equations are satisfied at every node which does not carry a boundary condition, and for nodes with boundary conditions the approximate solution or the derivative of the approximate solution are set to the given Dirichlet and Neumann boundary conditions, respectively. The point collocation approach gives rise to a linear system of equations, the solution of which gives the nodal parameters at nodes. Once the nodal parameters are computed, the unknown solution at each node can be computed from Eq. (20).

4. FCM for linear elasticity analysis

For two-dimensional elasticity, there are two unknowns associated with each node in the domain, namely, the

displacements in the x and y direction. In this paper we consider the plane strain situation. For an interior node, the governing equations, given in Eq. (1), are approximated by the fixed kernel interpolation given by Eqs. (22)–(26). For a node J, satisfying the equilibrium equation gives

$$\begin{cases} \dfrac{2(1-v)}{1-2v}\displaystyle\sum_{I=1}^{\mathrm{NP}}\frac{\partial^2 N_I(x_j,y_j)}{\partial x^2}\hat{u}_I + \frac{1}{1-2v}\sum_{I=1}^{\mathrm{NP}}\frac{\partial^2 N_I(x_j,y_j)}{\partial x\partial y}\hat{v}_I + \sum_{I=1}^{\mathrm{NP}}\frac{\partial^2 N_I(x_j,y_j)}{\partial y^2}\hat{u}_I = 0 \\ \dfrac{2(1-v)}{1-2v}\displaystyle\sum_{I=1}^{\mathrm{NP}}\frac{\partial^2 N_I(x_j,y_j)}{\partial x^2}\hat{v}_I + \frac{1}{1-2v}\sum_{I=1}^{\mathrm{NP}}\frac{\partial^2 N_I(x_j,y_j)}{\partial x\partial y}\hat{u}_I + \sum_{I=1}^{\mathrm{NP}}\frac{\partial^2 N_I(x_j,y_j)}{\partial y^2}\hat{v}_I = 0 \end{cases} \tag{27}$$

where (x_j, y_j) is the coordinate of node J and v is the Poisson's ratio.

For a node K with a Dirichlet boundary condition on the x-component of the displacement (e.g. $u^{\mathrm{a}} = g$), we obtain

$$\sum_{I=1}^{\mathrm{NP}} N_I(x_k, y_k)\hat{u}_I = g \tag{28}$$

where (x_k, y_k) is the location of node K.

Similarly, for a node L with a Neumann condition (e.g. $u^{\mathrm{a}}_x = h_x$), we obtain

$$\sum_{I=1}^{\mathrm{NP}} \frac{\partial N_I(x_1, y_1)}{\partial x}\hat{u}_I = h_x \tag{29}$$

where (x_1, y_1) is the coordinate of node L.

Combining Eqs. (27)–(29) for all the nodes, we obtain a linear system of equations, the solution of which gives the nodal parameters $\hat{u}_I$ and $\hat{v}_I$. Once the nodal parameters are known, the x- and y-displacements are computed by

$$u^{\mathrm{a}}(x,y) = \sum_{I=1}^{\mathrm{NP}} N_I(x,y)\hat{u}_I \tag{30}$$

$$v^{\mathrm{a}}(x,y) = \sum_{I=1}^{\mathrm{NP}} N_I(x,y)\hat{v}_I \tag{31}$$

5. FCM for nonlinear elasticity analysis

If an elastic body undergoes large deformation, linear theory is not valid and geometrically nonlinear elastic analysis needs to be employed. The governing equations for geometrically nonlinear analysis of micromechanical structures are stated in Eqs. (4)–(6). The displacements and their derivatives in Eqs. (4)–(6) are approximated by the meshless interpolations defined in Eqs. (20)–(26). The deformation gradient tensor can be rewritten as

$$\boldsymbol{F} = \begin{bmatrix} 1 + \sum_{I=1}^{\mathrm{NP}} \dfrac{\partial N_I(x,y)}{\partial X}\hat{u}_I & \sum_{I=1}^{\mathrm{NP}} \dfrac{\partial N_I(x,y)}{\partial Y}\hat{u}_I \\ \sum_{I=1}^{\mathrm{NP}} \dfrac{\partial N_I(x,y)}{\partial X}\hat{v}_I & 1 + \sum_{I=1}^{\mathrm{NP}} \dfrac{\partial N_I(x,y)}{\partial Y}\hat{v}_I \end{bmatrix} \tag{32}$$

Similarly, the stress and the strain tensors defined in Eqs. (8)–(10) can be approximated by the meshless interpolation functions. Approximating all the unknowns and their derivatives by the meshless interpolation functions and substituting them into Eq. (4), gives rise to a nonlinear system of equations of the form

$$\boldsymbol{f}_j(\hat{u}_1, \hat{u}_2, \ldots, \hat{u}_{\mathrm{NP}}, \hat{v}_1, \hat{v}_2, \ldots, \hat{v}_{\mathrm{NP}}) = 0, \quad j = 1, 2 \tag{33}$$

where $\boldsymbol{f}_1$ and $\boldsymbol{f}_2$ refer to the equilibrium equations in the x- and y-directions, respectively. The nonlinear system of equations is solved by employing a Newton's method. For nodes with Dirichlet and Neumann boundary conditions, the governing equations are

$$\boldsymbol{u}^{\mathrm{a}} - \boldsymbol{G} = 0 \text{ in } \Gamma_{\mathrm{g}} \tag{34}$$

$$\boldsymbol{P}(u^{\mathrm{a}})\boldsymbol{N} - \boldsymbol{H} = 0 \text{ in } \Gamma_{\mathrm{h}} \tag{35}$$

The accuracy of FCM is demonstrated by computing the large deformation of a cantilever beam. Fig. 2 shows the geometry and material properties of the cantilever beam. Fig. 3 shows the initial and the computed deformed configuration of the cantilever beam when subjected to a follower load. In Figs. 4 and 5, the results obtained with the meshless method for follower loads and vertical loads are compared with the analytical results and ANSYS results, respectively. The good match establishes the accuracy of the nonlinear meshless technique. In Fig. 6, we simulated the same beam with vertical loads by using a random distribution of 455 points. A comparison with the analytical solution is shown in Fig. 7. This result clearly demonstrates the significance of the method by simply sprinkling points randomly, we can obtain accurate results without having to go through the complex process of generating meshes. Furthermore, mesh distortion problem for large deformation analysis is eliminated by using FCM.

6. Electrostatic MEMS analysis

Analysis of electrostatic MEMS requires the coupled solution of mechanical and electrostatic equations [1,13]. In this paper, the mechanical deformations are computed by using either the linear theory (summarized in Eqs. (1)–(3)) or the nonlinear theory (summarized in Eqs. (4)–(6)) and the electrostatic forces are computed by the expression

$$\boldsymbol{h} = \frac{\varepsilon_0 V^2}{2g^2}\left(1 + 0.65\frac{g}{w}\right)\boldsymbol{n} \quad \text{for} \quad \text{linear theory} \tag{36}$$

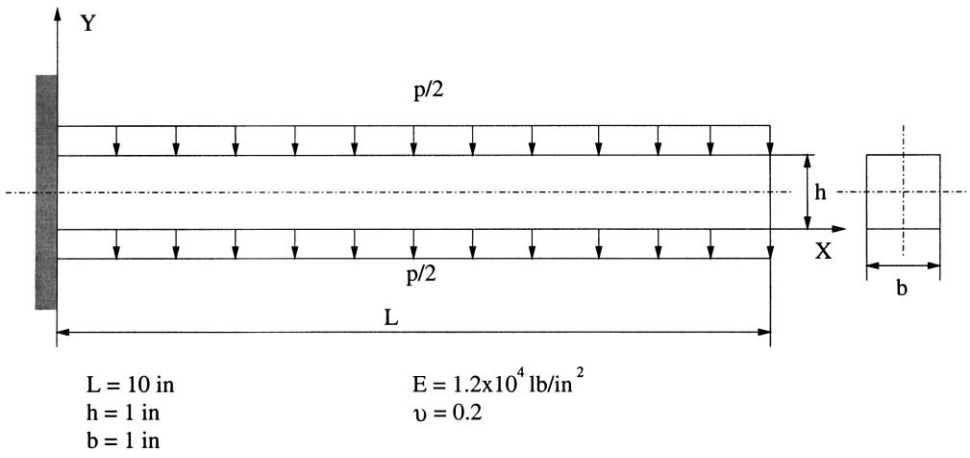

Fig. 2. Cantilever beam subjected to uniformly distributed load.

$$\boldsymbol{H} = \frac{\varepsilon_0 V^2}{2g^2}\left(1 + 0.65\frac{g}{w}\right)J\boldsymbol{F}^{-\mathrm{T}}\boldsymbol{N} \quad \text{for} \quad \text{nonlinear theory} \tag{37}$$

where ε_0 is the permittivity of free space, V the applied voltage, g the gap, w the width, $\boldsymbol{n}$ the surface normal of the beam, $\boldsymbol{N}$ the surface normal of the initial configuration of the beam, $\boldsymbol{F}$ the deformation gradient and J the determinant of $\boldsymbol{F}$.

To investigate the accuracy of linear and nonlinear theories for electrostatic MEMS, we focus on analysis of cantilever and fixed–fixed beams. The pull-in voltage of cantilever and fixed–fixed beams is an important variable for analysis and design of micro-switches and other micro-devices. Typically, the pull-in voltage is a function of geometry variables such as length, width, and thickness of the beam and the gap between the beam and the ground plane. While the pull-in voltage obtained with linear and nonlinear theories is identical when the geometric variables are within certain limits, it differs in other situations. The study in this section focuses on identifying the regimes where linear and nonlinear theories are accurate.

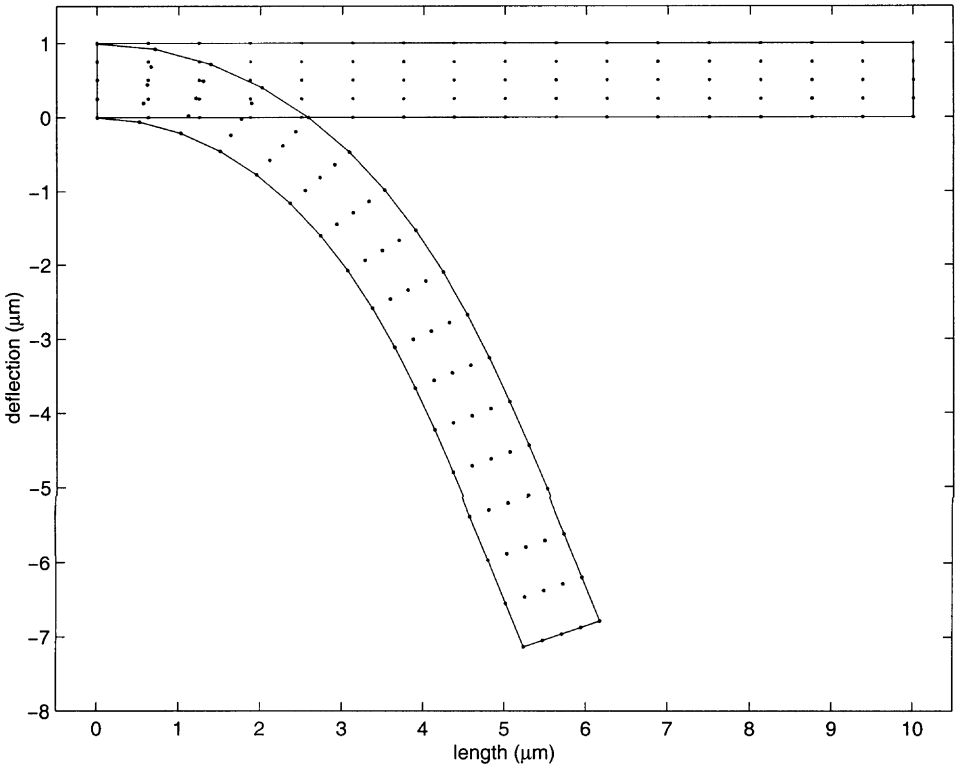

Fig. 3. Deformed cantilever beam using a uniform point distribution.

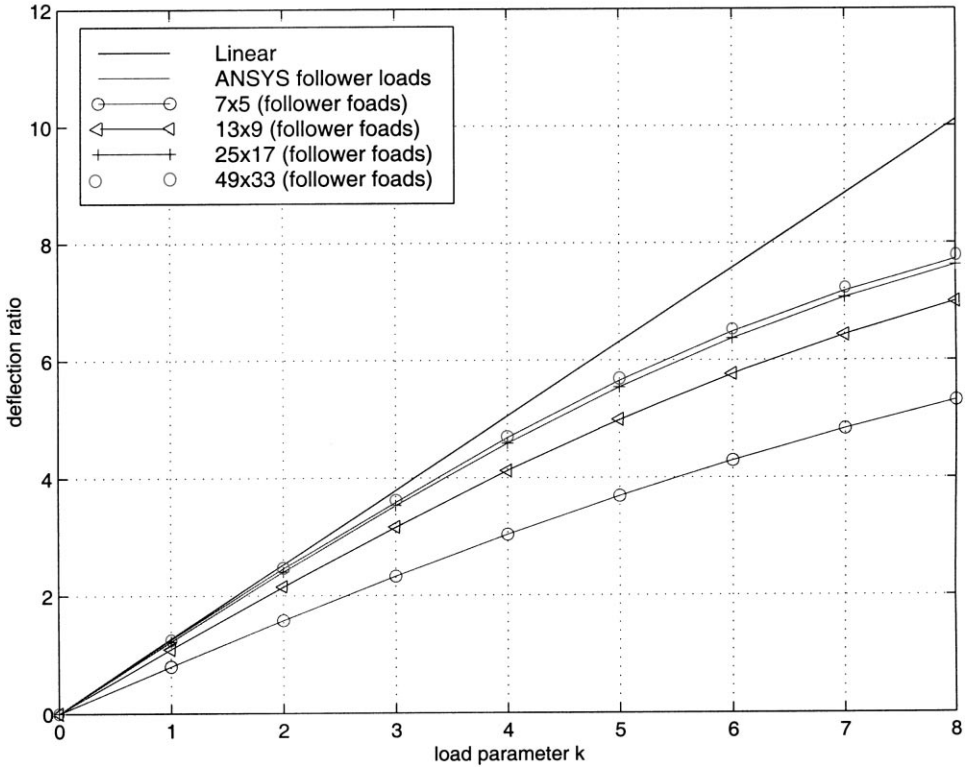

Fig. 4. Comparison of the meshless solution with the analytical solution for follower loads.

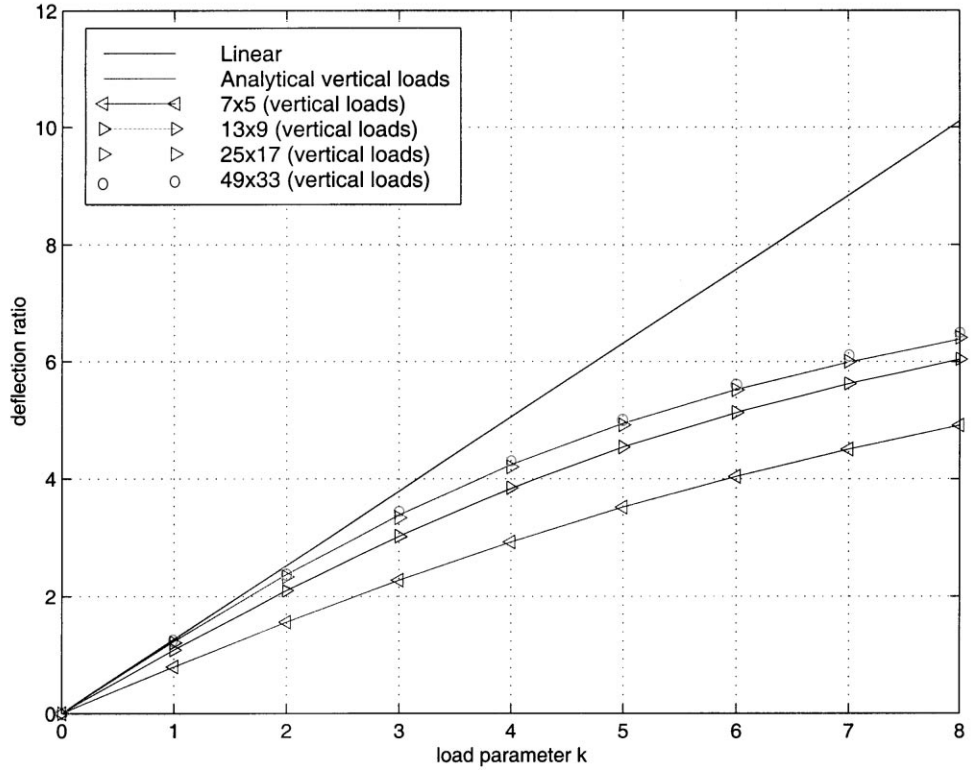

Fig. 5. Comparison of the meshless solution with the ANSYS solution for vertical loads.

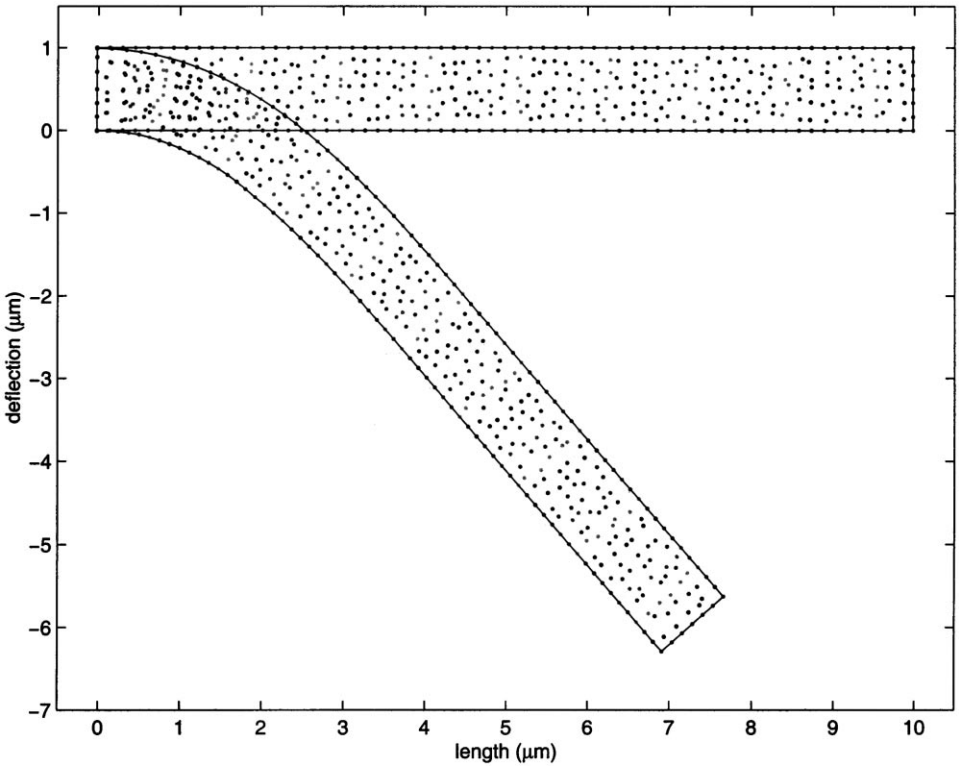

Fig. 6. Deformed cantilever beam using a random distribution of points.

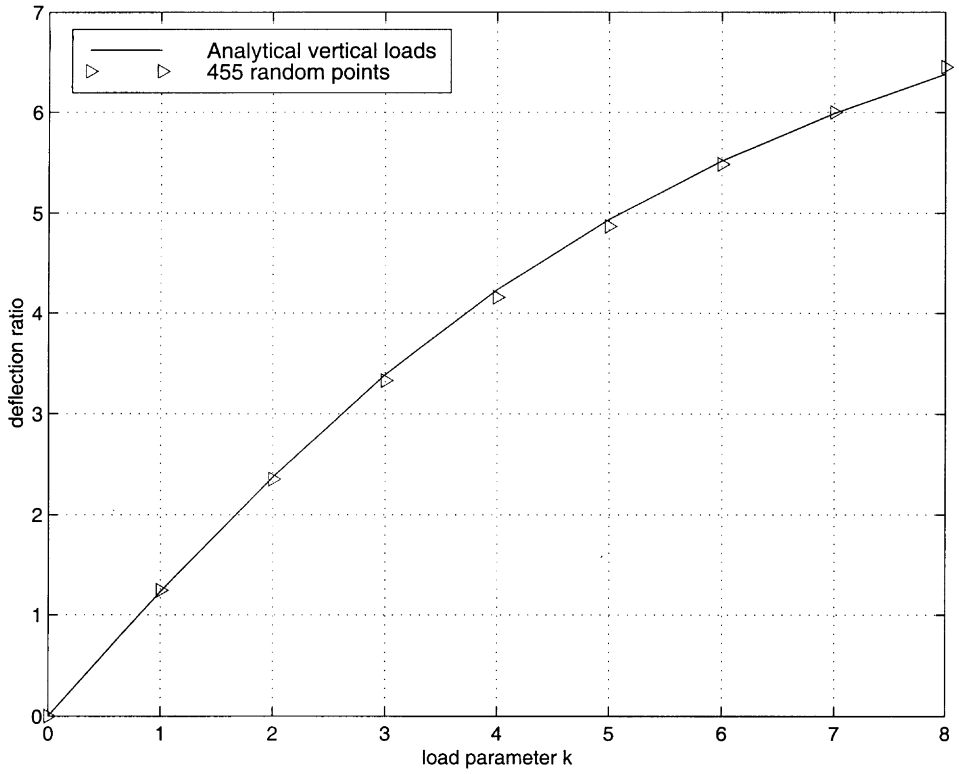

Fig. 7. Comparison of the meshless solution (obtained with a random distribution of points) with the analytical solution.

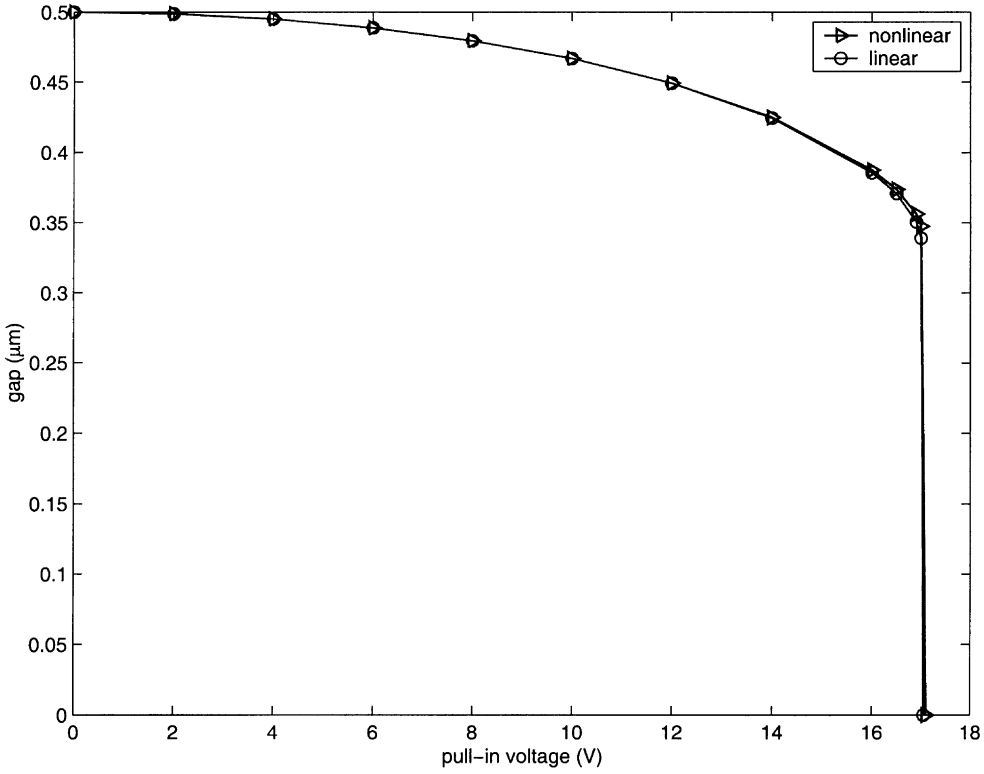

Fig. 8. Comparison of linear and nonlinear results for a fixed–fixed beam with a gap of 0.5 μm.

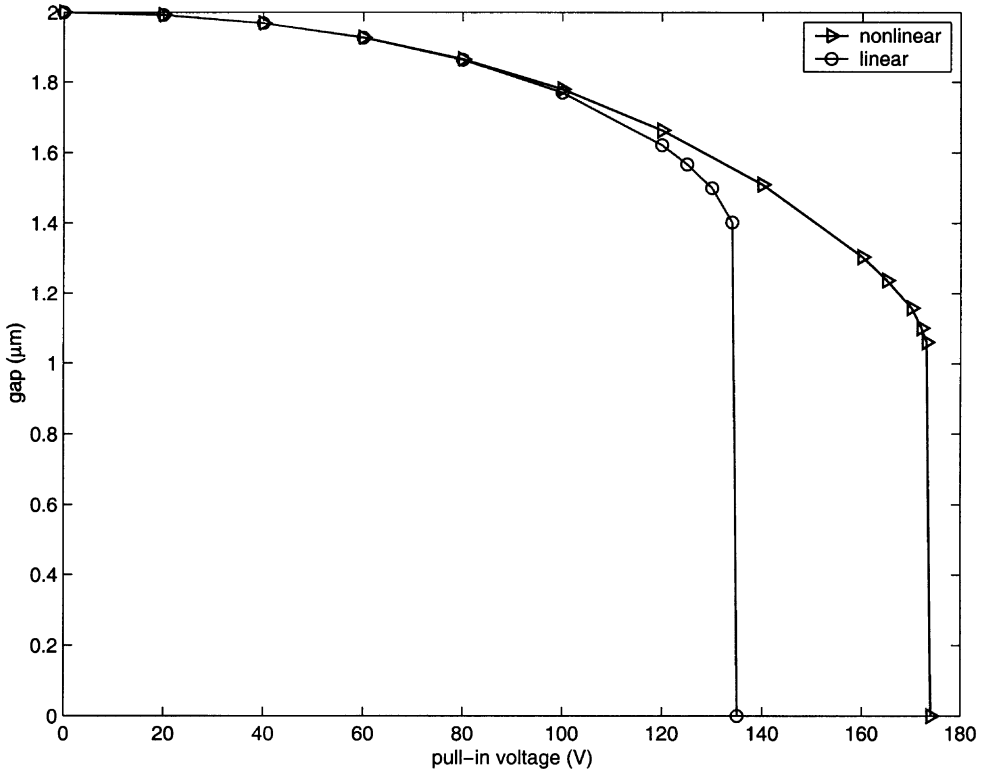

Fig. 9. Comparison of linear and nonlinear results for a fixed–fixed beam with a gap of 2 μm.

To highlight the differences between linear and nonlinear results, we first compare the peak deflection and pull-in voltage for a fixed–fixed beam with a length of 100 μm, a width of 50 μm, a thickness of 1 μm and two gap lengths. For a small gap length of 0.5 μm (shown in Fig. 8), we observe that both linear and nonlinear theories give identical results. However, for a large gap length of 2 μm (shown in Fig. 9), we observe that the pull-in voltage is significantly different. As shown in Fig. 10 , the difference in the pull-in voltage is even larger when a gap length of 4 μm is considered.

More extensive studies for the cantilever beam with lengths varying from 100 to 500 μm and thicknesses varying from 1 to 4 μm are shown in Figs. 11 and 12. The gap lengths used vary from 6 to 30 μm. For gaps smaller than 20 μm and lengths larger than 200 μm, we observe that the pull-in voltages obtained with both linear and nonlinear theories are very close. However, for large gaps (such as the 30 μm case) and for short beams (such as the 100 μm case), we observe that the difference in the pull-in voltage obtained with linear and nonlinear theories is not negligible. Fig. 13 shows the error between the two pull-in voltages. For beam lengths larger than 300 μm, the error is indistinguishable. The error is small for a length of 200 μm and when the beam length gets shorter (such as 100 μm), the error starts becoming significant. From Fig. 13, we also observe that the thickness has very little effect on the error compared to the effect of gap and length, although the thicker the beam, the higher the pull-in voltage.

In Figs. 14–16, we investigate the fixed–fixed beam example with lengths varying from 100 to 500 μm and thicknesses varying from 0.5 to 2 μm. We observe that, for all cases, the pull-in voltages obtained with linear theories are in significant error (larger than 10%) compared to the pull-in voltages obtained with nonlinear theories. When the gap increases, the error in pull-in voltage with linear theory increases significantly. Furthermore, contrary to the case of cantilever beams, the thickness has a significant effect on the error in pull-in voltages. The thinner the beam, the larger the error. Another observation is that the length of the beam has little effect on the error in the pull-in voltage. This observation is also different from the case of cantilever beams. From the results, it is clear that linear theory is generally not valid for the fixed–fixed beam case, except when the gap is very small, such as the 0.5 μm case as shown in Fig. 8.

7. Mixed-regime analysis

The results in Section 6 indicate that linear theory is not valid for certain cases. Nonlinear theory can be used reliably under all cases, however, the use of nonlinear theory in situations where the linear theory is adequate can be

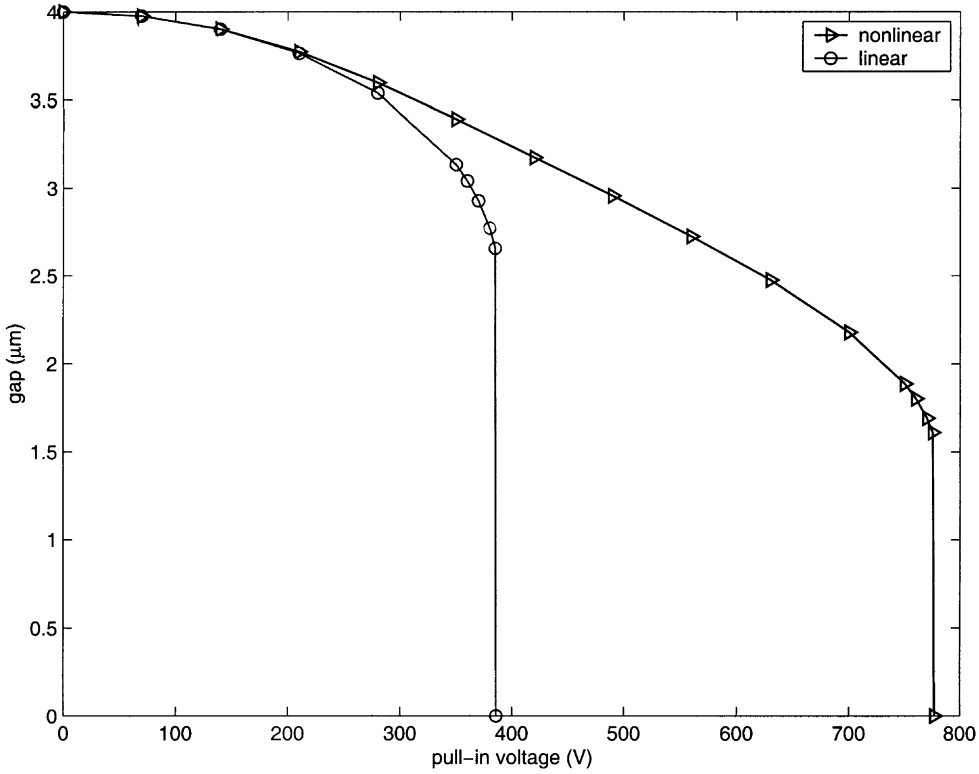

Fig. 10. Comparison of linear and nonlinear results for a fixed–fixed beam with a gap of 4 μm.

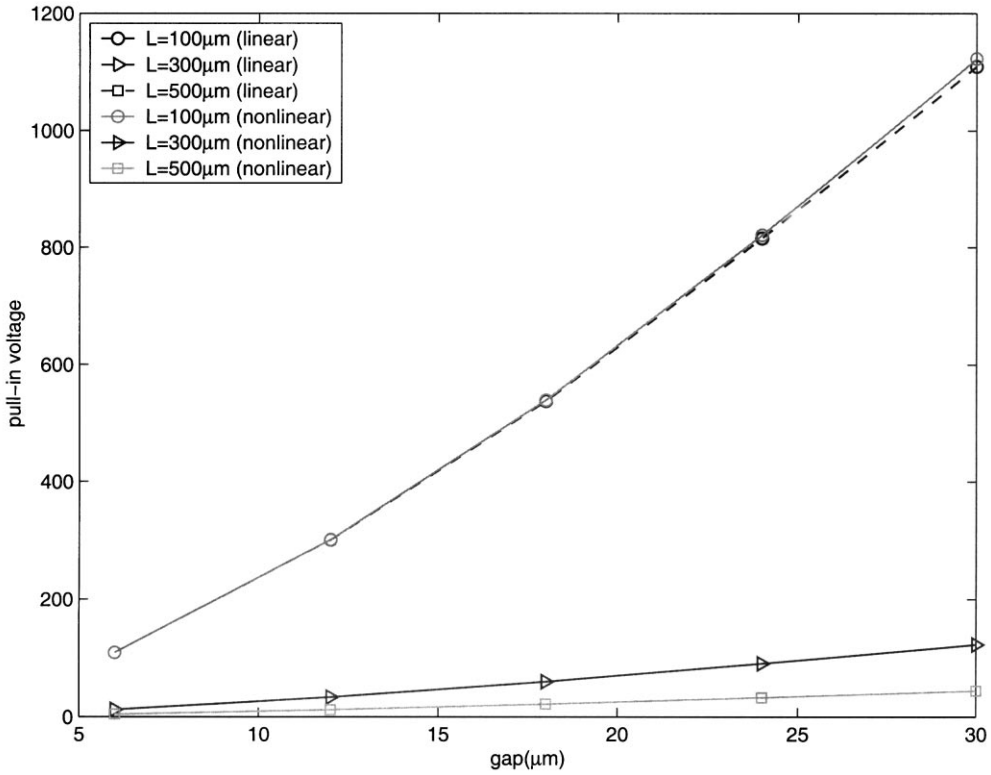

Fig. 11. Gap vs. pull-in voltage for cantilever beams with a thickness of 1 μm. For length = 100 μm, the difference in pull-in voltage between linear and nonlinear theories is significant when the gap is larger than 20 μm. For a length larger than 300 μm, the pull-in voltages obtained with linear and nonlinear theories are identical.

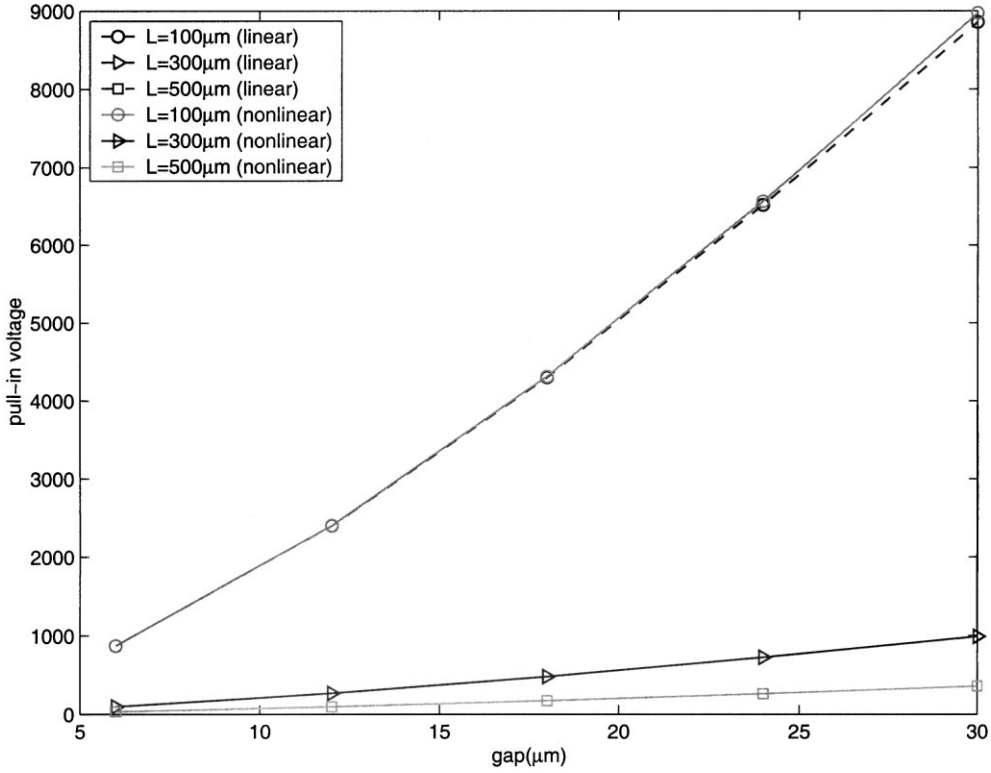

Fig. 12. Gap vs. pull-in voltage for cantilever beams with a thickness of 4 μm. Similar to Fig. 11, for length = 100 μm, the difference in pull-in voltage between linear and nonlinear theories is significant when the gap is larger than 20 μm. For a length larger than 300 μm, the pull-in voltages obtained with linear and nonlinear theories are identical.

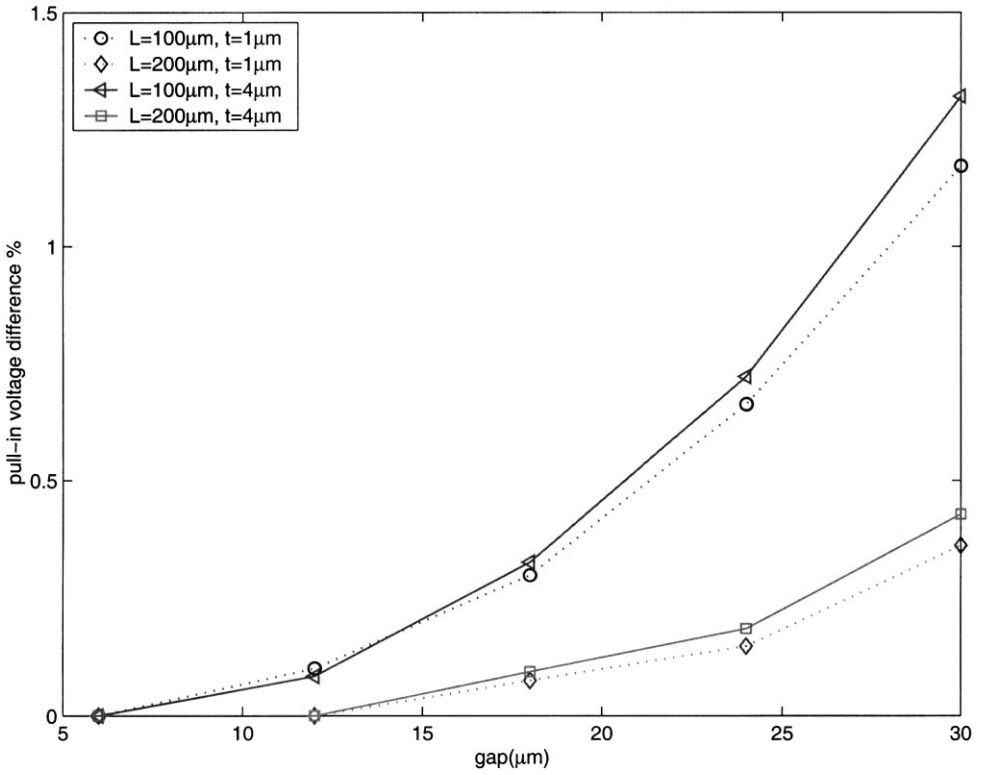

Fig. 13. Gap vs. difference in pull-in voltage between linear and nonlinear theories for cantilever beams.

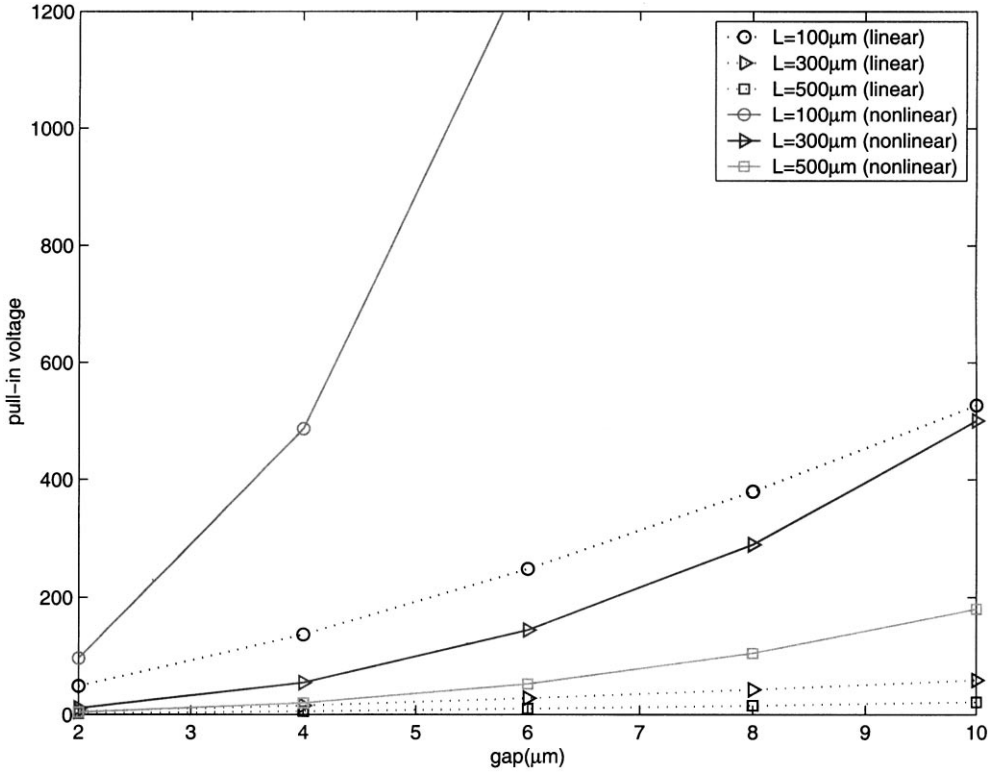

Fig. 14. Gap vs. pull-in voltage for fixed–fixed beams with a thickness of 0.5 μm. Observe the large difference in pull-in voltages obtained from linear and nonlinear theories.

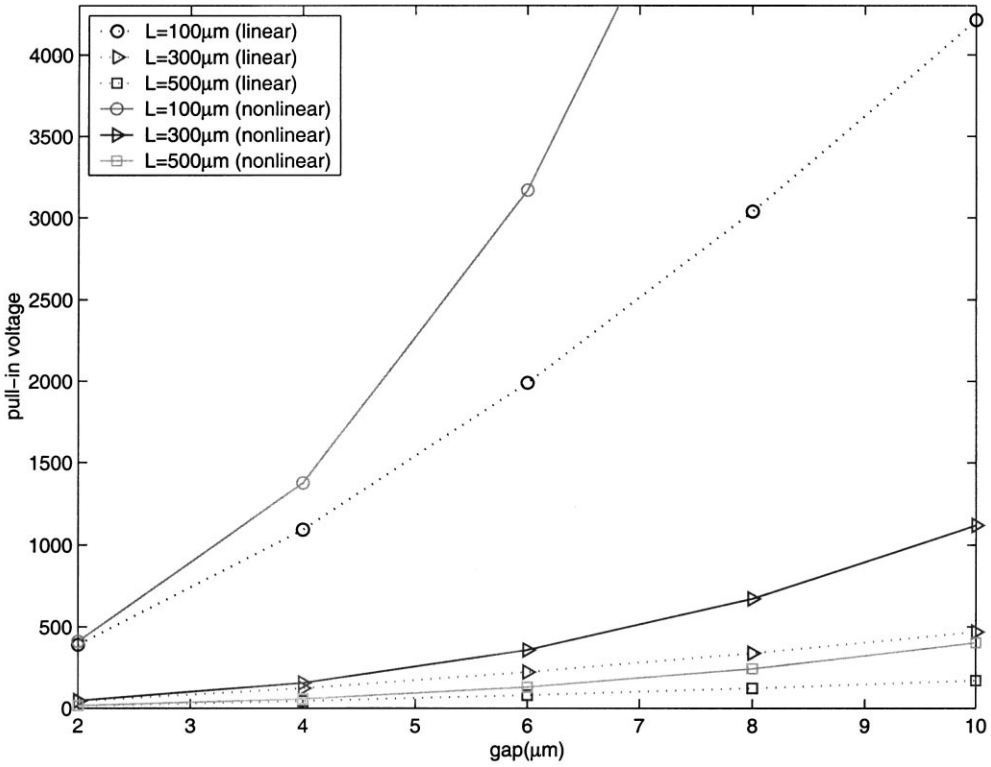

Fig. 15. Gap vs. pull-in voltage for fixed–fixed beams with a thickness of 2 μm. Similar to Fig. 14, there is a large difference in pull-in voltages obtained from linear and nonlinear theories.

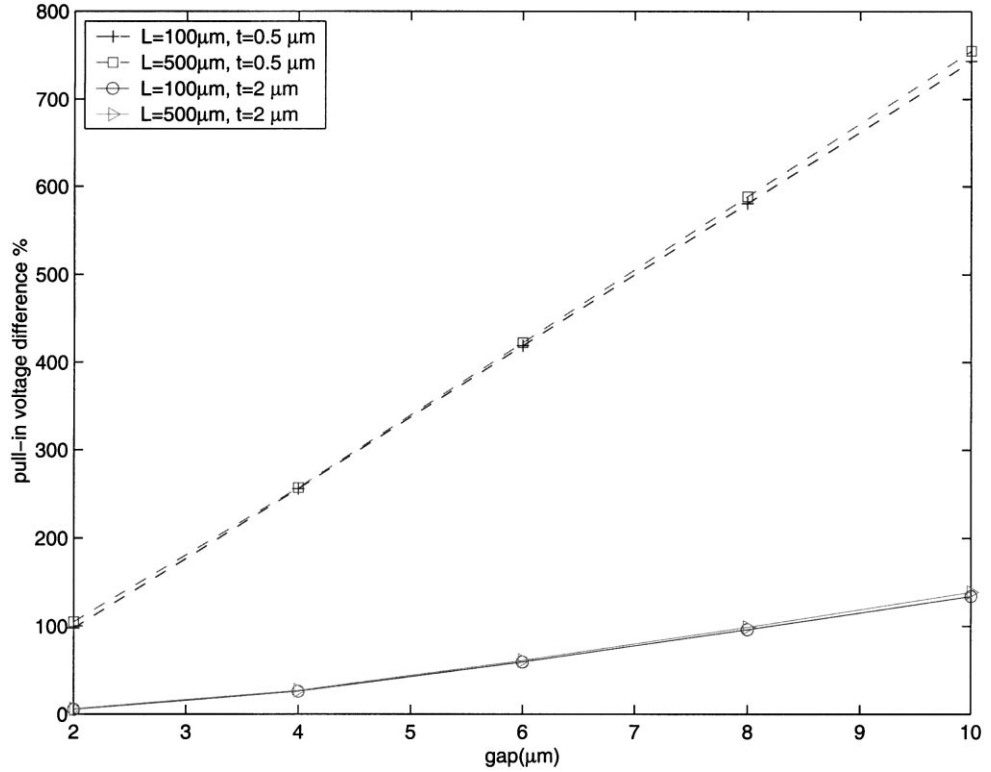

Fig. 16. Gap vs. difference in pull-in voltage between linear and nonlinear theories for fixed–fixed beams. Both gap and thickness have a significant effect on the difference in pull-in voltage. When the gap increases, the difference increases rapidly. When the thickness increases, the difference decreases. Length has small effect compared to the gap and thickness.

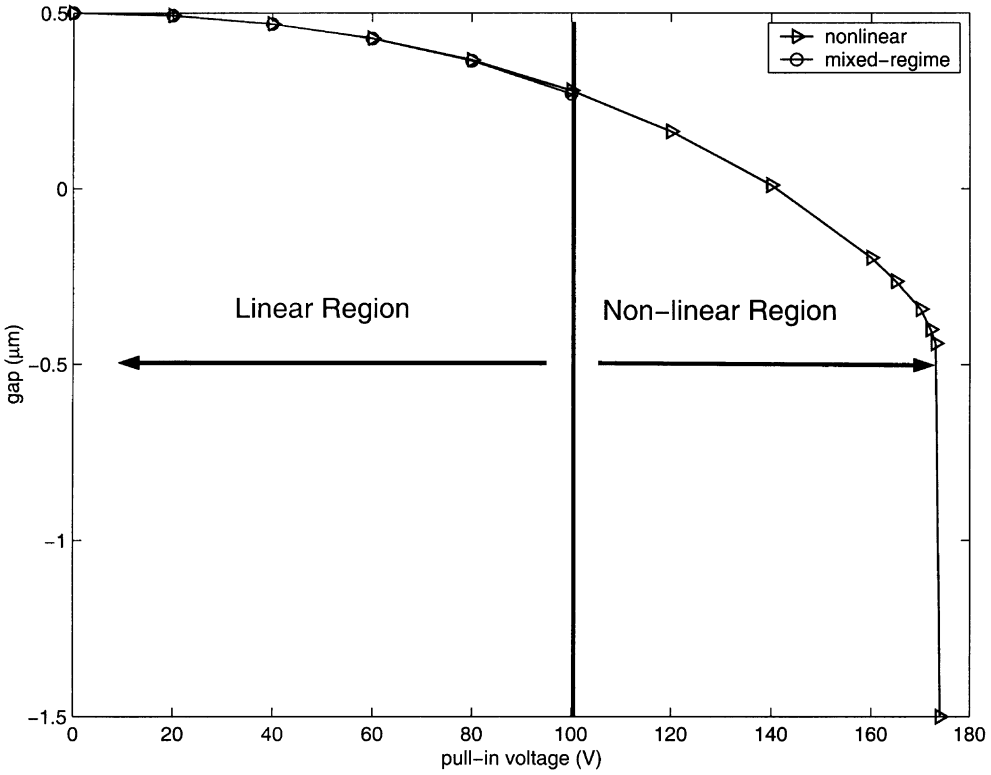

Fig. 17. Mixed-regime simulation. Linear theory is applied for the linear region (small voltages) and nonlinear theory is applied for the nonlinear region (large voltages).

expensive, complicated and time consuming. As shown in Fig. 9, the linear and nonlinear theories give identical results upto a certain applied voltage (say V_1) and beyond V_1 the deflection curves with both theories start to deviate. The final result is a significant difference in pull-in voltage between the two theories. An efficient approach to address this problem is to use a mixed-regime technique, where a linear theory will be employed upto V_1 and a nonlinear theory will be employed beyond V_1.

The mixed-regime technique is demonstrated for the example shown in Fig. 9. Thirteen load steps (or voltage increments) are used to get the pull-in voltage. The first five load steps are computed using the linear theory and the remaining eight load steps are computed using the nonlinear theory. The results with the mixed-regime approach are shown in Fig. 17. For each load step, the CPU time is about 1.5 s for linear analysis and 7.8 s for nonlinear analysis. Thus, the mixed-regime approach is about 30% faster compared to the use of the full nonlinear theory for prediction of pull-in voltage.

A critical issue that needs to be addressed for the mixed-regime approach is to identify the voltage V_1. Several criteria can be employed to determine V_1. We propose the following three strategies.

1. For each load step, compute both the Green's strain tensor and the engineering strain tensor. When the difference between the entries of the two strain tensors is larger than 1%, nonlinear theory must be employed.
2. For each load step, compute the engineering strains and the rotation. When either of these variables is larger than 1%, nonlinear theory must be employed.
3. For each load step, investigate the peak deflection of the beam. When the peak deflection is larger than 20% of the thickness of the beam, nonlinear theory must be employed.

For implementation purposes, one can use any combination of these criteria to obtain the voltage V_1.

8. Conclusions

The primary contributions of the paper are summarized as follows.

1. For cantilever beams, linear theories hold over a regime, where the gap is not very large (gap less than 20% of the beam length). For fixed–fixed beams, linear theories hold over a very small regime (gap less than 0.5 μm). For accurate simulations or for the development of reduced-order models, designers need to use nonlinear theories appropriately.
2. For cantilever beams, length has a significant effect on the error in pull-in voltages, while for fixed–fixed

beams, the length has little effect on the error. On the other hand, for fixed–fixed beams, thickness has significant effect on the error in pull-in voltage, while for cantilever beams it has little effect.

3. A mixed-regime simulation approach has been implemented to reduce the computational cost while maintaining the accuracy of nonlinear simulation.
4. We have also introduced new nonlinear meshless techniques to efficiently and accurately simulate the nonlinear behavior of electrostatic devices. These approaches offer radically simpler and easy-to-use CAD tools for MEMS designers.

Acknowledgements

This work was supported by an NSF CAREER award to N.R. Aluru and by a grant from DARPA under agreement number F30602-98-2-0178. This support is gratefully acknowledged.

References

[1] N.R. Aluru, J. White, An efficient numerical technique for electromechanical simulation of complicated microelectromechanical structures, Sens. Actuat. A 58 (1997) 1–11.

[2] J.R. Gilbert, R. Legtenberg, S.D. Senturia, 3-D coupled electromechanics for MEMS: applications of CoSolve-EM, in: Proceedings of the MEMS, 1995, pp. 122–127.

[3] Y. Chen, J. White, A quadratic method for nonlinear model order reduction, in: Proceedings of the MSM, 2000, pp. 477–480.

[4] E.S. Hung, S.D. Senturia, Generating efficient dynamical models for microelectromechanical systems from a few finite-element simulation runs, J. Microelectromech. Syst. 8 (3) (1999) 280–289.

[5] G.E. Forsythe, W.R. Wasow, Finite Difference Methods for Partial Differential Equations, Wiley, New York, 1960.

[6] T.J.R. Hughes, The Finite Element Method: Linear Static and Dynamic Finite Element Analysis, Prentice-Hall, Englewood Cliffs, NJ, 1987.

[7] N.R. Aluru, G. Li, Finite cloud method: a true meshless technique based on a fixed reproducing Kernel approximation, Int. J. Numerical Methods Eng. 50 (10) (2001) 2373–2410.

[8] N.R. Aluru, A point collocation method based on reproducing Kernel approximations, Int. J. Numerical Methods Eng. 47 (2000) 1083–1121.

[9] N.R. Aluru, A reproducing Kernel particle method for meshless analysis of microelectromechanical systems, Computational Mechanics 23 (1999) 324–338.

[10] K.J. Bathe, E. Ramm, E.L. Wilson, Finite element formulations for large deformation dynamic analysis, Int. J. Numerical Methods Eng. 9 (1975) 353–386.

[11] P.M. Osterberg, S.D. Senturia, *M*-test: a test chip for MEMS material property measurement using electrostatically actuated test structures, J. Microelectromech. Syst. 6 (2) (1997) 107–118.

[12] L.E. Malvern, Introduction to the Mechanics of Continuum Medium, Prentice-Hall, Englewood Cliffs, NJ, 1969.

[13] N.R. Aluru, J. White, A multilevel Newton method for mixed-energy domain simulation of MEMS, J. Microelectromech. Syst. 8 (3) (1999) 299–308.